

Chemical Science

Accepted Manuscript

This article can be cited before page numbers have been issued, to do this please use: B. Ge, Y. Chen, Y. Wu, F. Wei, F. Li, L. Chen, J. Lin, X. Fu and S. Lin, *Chem. Sci.*, 2026, DOI: 10.1039/D6SC01740A.



This is an Accepted Manuscript, which has been through the Royal Society of Chemistry peer review process and has been accepted for publication.

Accepted Manuscripts are published online shortly after acceptance, before technical editing, formatting and proof reading. Using this free service, authors can make their results available to the community, in citable form, before we publish the edited article. We will replace this Accepted Manuscript with the edited and formatted Advance Article as soon as it is available.

You can find more information about Accepted Manuscripts in the [Information for Authors](#).

Please note that technical editing may introduce minor changes to the text and/or graphics, which may alter content. The journal's standard [Terms & Conditions](#) and the [Ethical guidelines](#) still apply. In no event shall the Royal Society of Chemistry be held responsible for any errors or omissions in this Accepted Manuscript or any consequences arising from the use of any information it contains.

Data-Driven Structural Angle Mining Elucidates Hidden Design

Rules for Hydrogen Evolution Single-Atom Electrocatalysts

Bingqing Ge^{+acd}, Yang Chen^{+b}, Yidi Wu^{+ac}, Fenfei Wei^{cd}, Fengyu Li^f, Lulu Chen^{ac}, Jian Lin^{*b},
Xianzhi Fu^{ac} and Sen Lin^{*ace}

^aState Key Laboratory of Chemistry for NBC Hazards Protection, College of Chemistry, Fuzhou University, Fuzhou 350116, China

^bCAS Key Laboratory of Science and Technology on Applied Catalysis, Dalian Institute of Chemical Physics, Chinese Academy of Sciences, Dalian 116023, China

^cState Key Laboratory of Photocatalysis on Energy and Environment, College of Chemistry, Fuzhou University, Fuzhou 350002 China

^dKey Laboratory of Mesoscopic Chemistry, School of Chemistry, Nanjing University, Nanjing 210023, Jiangsu, China

^eCollege of Chemistry and Chemical Engineering, Institute for Green Chemistry and Environmental Science, Inner Mongolia University, Hohhot 010021, China

^fResearch Center for Quantum Physics and Technologies, School of Physical Science and Technology, Inner Mongolia University, Hohhot, 010021, China

⁺These authors contributed equally to this work.

*Email: jianlin@dicp.ac.cn, slin@fzu.edu.cn



27 **Abstract:** Structural distortions in modified two-dimensional transition metal dichalcogenides
28 (MX_2) influence electrocatalytic activity, yet quantitative and predictive structure-property
29 relationships remain underdeveloped. To bridge this gap, we perform data-driven structural angle
30 mining across hundreds of thousands of single-atom doped configurations ($\text{TM}_1@MX_2$) and
31 establish geometrically defined angular descriptors. These descriptors exhibit high predictive
32 accuracy for hydrogen evolution electrocatalysis. Crucially, our analysis reveals that catalytic
33 activity correlates more strongly with long-range angular parameters describing peripheral
34 geometric effects than with the local coordination environment. Guided by these descriptors, we
35 identify specific angular signatures as quantitative predictors for high-performance catalysts: an
36 outer-shell S-centered angle indicates optimal hydrogen evolution reaction (HER) activity for
37 $\text{Ir}_1@MoS_2$ (S-vacancy), while a distinct Mo-centered angle identified $\text{V}_1@MoS_2$ (Mo-vacancy)
38 as a promising earth-abundant candidate. Experimental verification confirms these predictions:
39 synthesized $\text{Ir}_1@MoS_2$, with an ultralow loading of 0.1 wt%, achieves performance comparable
40 to commercial Pt/C on a mass-activity basis, while $\text{V}_1@MoS_2$ enhances HER performance
41 relative to pristine MoS_2 . The framework also shows strong computational correlations with
42 oxygen evolution activity, though experimental validation for OER remains an important
43 direction for future investigation. The angular descriptor framework introduced here provides a
44 geometrically intuitive and electronically grounded strategy for the rational design and accelerated
45 discovery of advanced energy materials.

46 **Keywords:** Hydrogen evolution electrocatalyst; Data-driven; Machine learning; Transition metal
47 dichalcogenide; Structural descriptor

48



49 Introduction

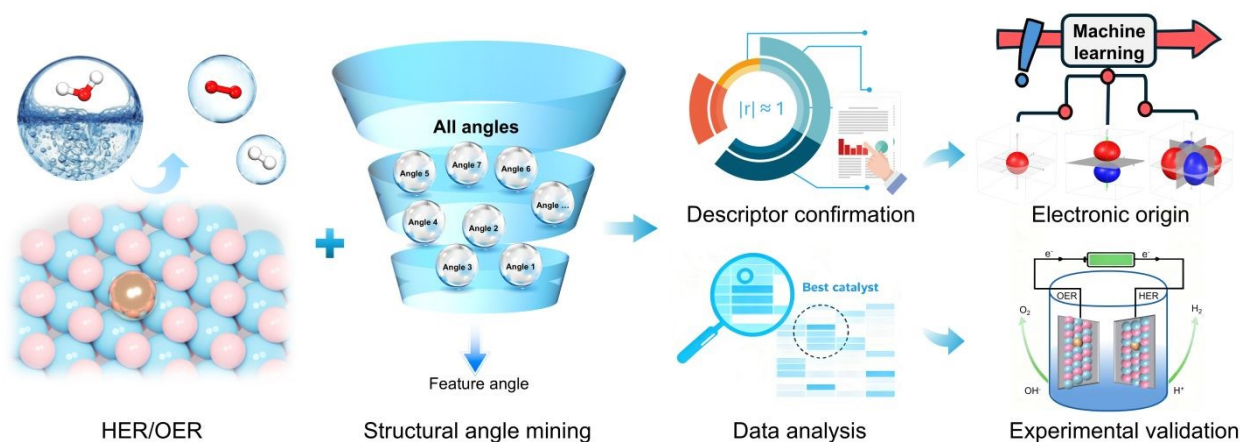
50 The transition to a sustainable energy future is contingent on the development of efficient
51 electrocatalysts for water splitting, a key technology for green hydrogen production. However,
52 widespread deployment of electrolyzers remains constrained by their reliance on scarce platinum-
53 group metals, spurring the search for earth-abundant alternatives without compromising activity.^{1–}
54 ⁴ While single-atom catalysts (SACs) embedded in two-dimensional transition metal
55 dichalcogenides (TM₁@MX₂) present a promising platform to reduce reliance on platinum-group
56 metals, their rational design remains fundamentally challenging.^{5–8} The catalytic performance is
57 exquisitely sensitive to the local atomic environment, where subtle structural distortions can
58 dramatically modulate activity.^{9–14} However, a critical gap persists between observing these
59 structural effects and quantitatively predicting them, as current paradigms struggle to decouple
60 the intricate interplay between geometry and electronic structure.

61 The descriptor-based approach, central to modern catalyst design, has long been dominated
62 by electronic structure parameters, such as adsorption energies and *d*-band centers.^{15–20} While
63 powerful, these descriptors often serve as computational proxies that are notoriously difficult to
64 translate into actionable synthesis guidelines. There exists a critical gap between the abstract
65 electronic parameters and the tangible geometric structures that chemists manipulate. They answer
66 the “what” but not the “how”, failing to provide experimentalists with clear geometric blueprints
67 for catalyst creation. Structural descriptors present a compelling alternative,^{21–23} with concepts
68 such as “surface distortion” successfully bridging structure-activity relationships across
69 nanocatalysts.²⁴ However, such ensemble-averaged structural probes, while insightful, lack the
70 atomic-scale resolution to pinpoint the specific geometric motifs that govern function. This gap
71 between macroscopic observation and atomic-scale design underscores the critical lack of an
72 intuitive, quantitative language to link synthesis to performance.

73 Efforts to establish such a language by directly linking three-dimensional atomic structure to
74 activity face significant challenges. Pioneering work has highlighted the role of local geometry,
75 using parameters like bond lengths.²⁵ Despite their utility, such one-dimensional metrics are
76 inherently limited in capturing the multidimensional nature of structural distortion.^{26–28} Similarly,
77 coordination numbers often oversimplify the complex, anisotropic coordination environment,
78 failing to resolve critical features beyond the first shell.^{29–33} Thus, the pressing need is for
79 multidimensional geometric descriptors that are synthetically interpretable yet rich enough to
80 encode the complexity of atomic-scale environments and to predict their catalytic function.



81 Here, we introduce data-driven angular descriptors to meet this pressing need. Unlike
 82 conventional approaches, these geometric parameters serve as a direct quantitative bridge between
 83 the synthesis-induced lattice strain and the resulting catalytic function. We demonstrate that
 84 catalytic activity is governed not merely by the local dopant identity, but by the precise angular
 85 distortions in the coordination shells. As outlined in Scheme 1, our integrated workflow
 86 progresses from data-driven descriptor mining to experimental validation. Through high-
 87 throughput density functional theory (DFT) screening of hundreds of thousands of $\text{TM}_1\text{@MX}_2$
 88 configurations, we establish that catalytic activity is governed not by the local coordination, but
 89 by long-range peripheral angles, geometric parameters that are both highly predictive and
 90 synthetically interpretable. Crucially, we decode how macroscopic lattice strain manifests in these
 91 specific angular motifs, a relationship that shows good transferability across reactions (hydrogen
 92 evolution reaction, HER, and oxygen evolution reaction, OER) and materials. Guided by this
 93 principle, we discover and experimentally validate two high-performance catalysts: an ultralow-
 94 loading $\text{Ir}_1\text{@MoS}_2$ competitive with Pt/C and an earth-abundant $\text{V}_1\text{@MoS}_2$. Thereby, we establish
 95 angular descriptors as a transformative tool, providing a quantitative, geometry-driven blueprint
 96 for rational catalyst design.



97
 98 **Scheme 1** Integrated workflow from data-driven angular descriptor mining to experimental
 99 validation of high-performance water splitting electrocatalyst.

100

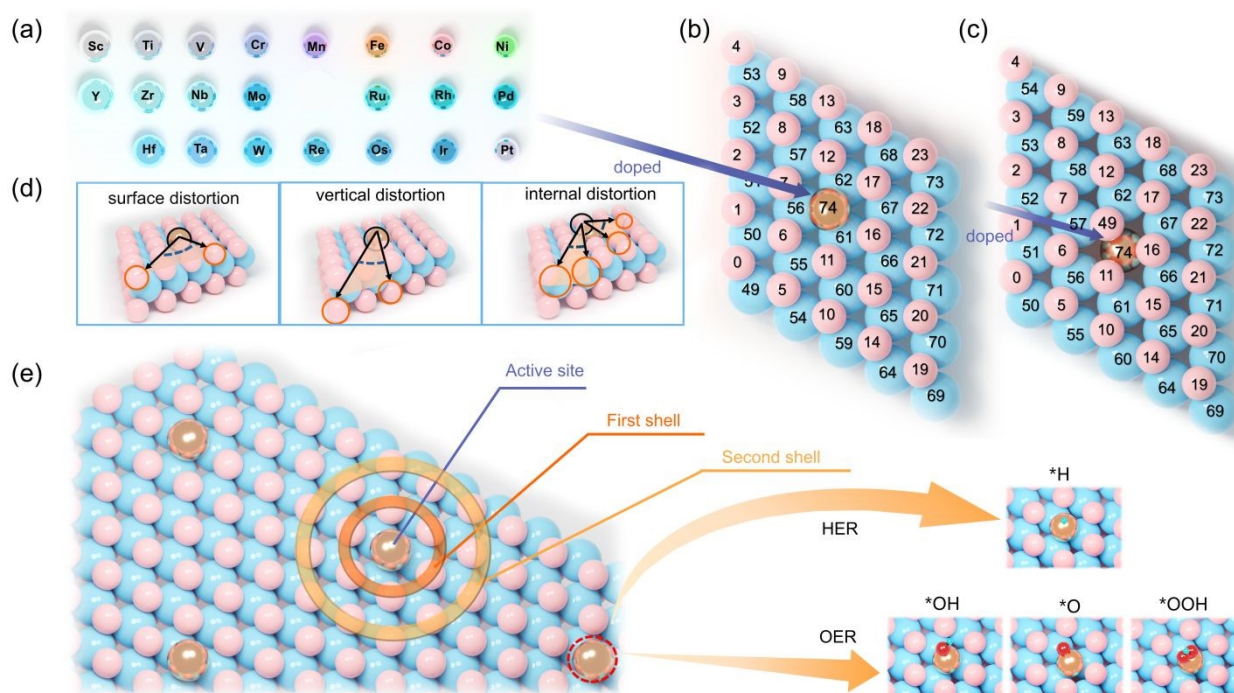
101 Results

102 Structural Angular Features

103 Guided by established experimental frameworks,^{34,35} and motivated by the well-recognized
 104 catalytic activity of MoS_2 for water electrolysis,^{36–39} we systematically investigate two distinct
 105 classes of $\text{TM}_1\text{@MX}_2$ systems classified by vacancy type: chalcogen-vacancy ($\text{TM}_1\text{@MX}_2\text{-X}$)



106 and metal-vacancy ($\text{TM}_1@MX_2\text{-M}$). Our study encompasses 22 transition metal dopants spanning
 107 the 3d, 4d, and 5d series (Figure 1a), providing broad chemical space exploration while excluding
 108 Tc and Hg for safety considerations and Cu, Ag, and Au due to their known catalytic inertness.^{40–}
 109 ⁴² In $\text{TM}_1@MX_2\text{-X}$ systems, each dopant atom occupies an S/Se vacancy site, forming three-fold
 110 coordination with three adjacent metal atoms (Figure 1b and Figure S1). Conversely, for
 111 $\text{TM}_1@MX_2\text{-M}$, each dopant atom occupies an Mo/W vacancy site and adopts six-fold
 112 coordination with surrounding chalcogen atoms (Figure 1c and Figure S2).



113
 114 **Figure 1.** (a) Periodic table highlighting the 22 transition metal dopants (3d/4d/5d) investigated
 115 in this study. (b) Atomic labeling scheme for $\text{TM}_1@MX_2\text{-X}$: top-layer chalcogens (S/Se, atoms
 116 0-23), bottom-layer chalcogens (24-48), host metal atoms ($M=\text{Mo/W}$, 49-73), and dopant
 117 transition metal (TM, atom 74). (c) Atomic labeling for $\text{TM}_1@MX_2\text{-M}$: top-layer chalcogens (0-
 118 23, 49), bottom-layer chalcogens (24-48), host metals (50-73), and dopant (74). (d) Three
 119 characteristic distortion modes: surface distortion (angle between vertex and top S/Se atom),
 120 vertical distortion (angle between vertex and interlayer S/Se axis), and internal distortion (angle
 121 between central Mo/W atom and vertex). (e) Active site geometry in $\text{TM}_1@MX_2\text{-X}$, showing the
 122 doped TM center coordinating key reaction intermediates (*H, *O, *OH, *OOH) for HER/OER
 123 processes. The corresponding HER active site configuration for $\text{TM}_1@MX_2\text{-M}$ is provided in
 124 Figure S3. Color scheme: blue = Mo/W atoms, pink = S/Se atoms, gold = dopant atoms.

125



126 The critical role of structural distortions in modulating catalytic performance is well
127 recognized, and dopant-induced lattice distortions are known to perturb electronic structure and
128 influence activity.^{43,44} While structural distortion descriptors are gaining attention for accelerating
129 structure-performance understanding,^{24,45} more intuitive geometric parameters are still needed.
130 Given that all macroscopic properties originate from atomic arrangements, we identify angular
131 distortions as particularly sensitive metrics for quantifying structure-activity relationships.

132 Our analysis reveals three fundamental angular distortion modes that define the structural
133 landscape (Figure 1d): surface distortion, characterizing top-layer geometry; vertical distortion,
134 capturing interlayer interactions; and internal distortion, describing core structural perturbations.
135 Doping-induced variations generate over 190,000 angular configurations per catalyst model,
136 enabling thorough quantification of local geometry.

137 The microstructure of metal-doped catalysts exhibits well-defined shell environments
138 (Figure 1e). In $\text{TM}_1\text{@MX}_2\text{-X}$ systems, the active site resides at the doped transition metal center,
139 where ligand atoms form concentric shell environments, including the first shell, the second shell,
140 and peripheral shells that coordinate key intermediates (*H, *O, *OH, *OOH) during HER and
141 OER. Different metal dopants induce characteristic distortions across these shell structures,
142 ultimately governing catalytic performance. A similar shell distortion mechanism operates in
143 $\text{TM}_1\text{@MX}_2\text{-M}$ systems, though the active center shifts to adjacent chalcogen sites (Figure S3).

144 **Data-Driven Development of Angular Descriptor for HER**

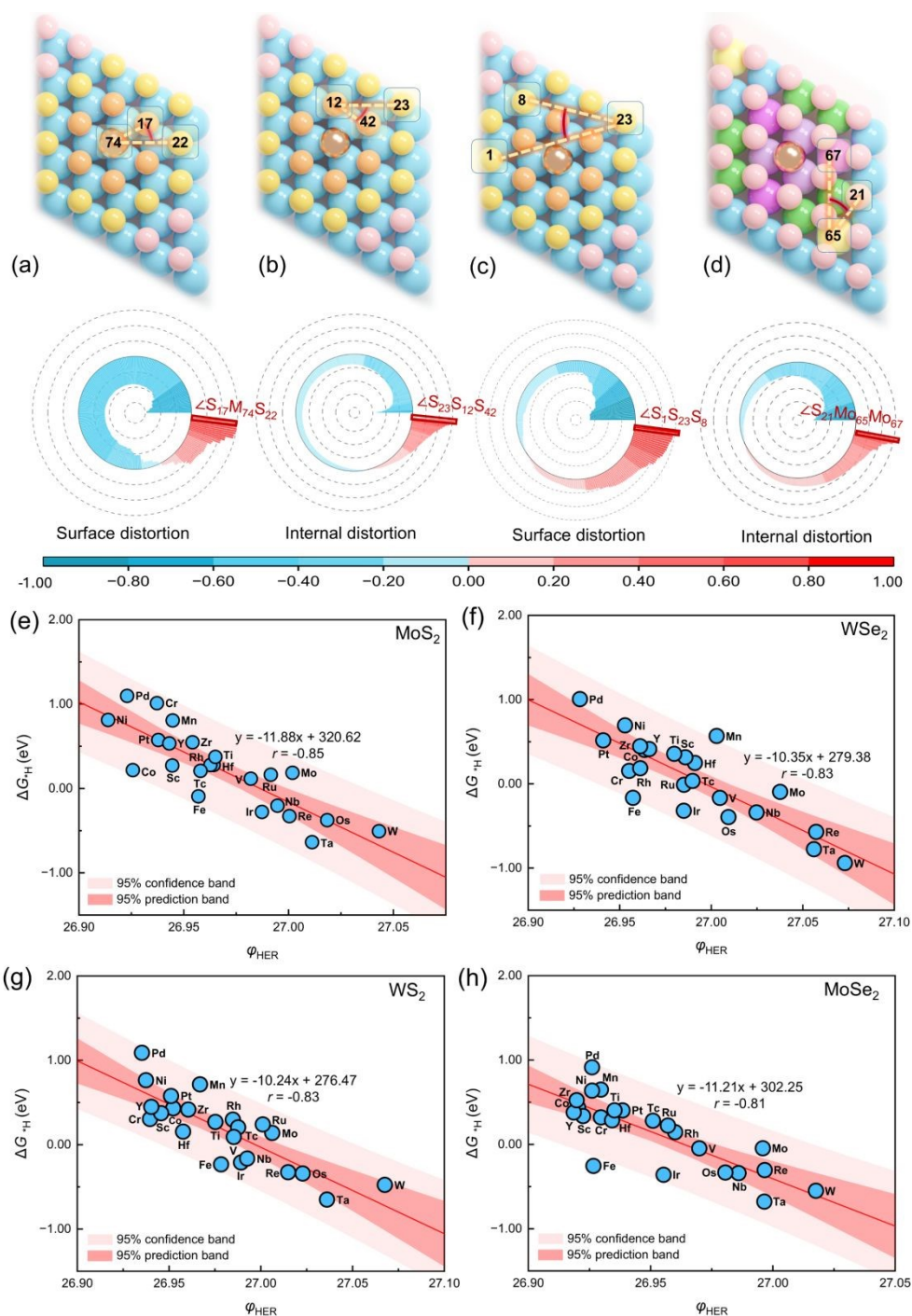
145 To establish quantitative structure-activity relationships for HER, we initially focus on
146 $\text{TM}_1\text{@MoS}_2\text{-X}$ as a model system. We start by systematically extracting all structural angles
147 centered at the dopant metal site, defined as the angle formed by the dopant and any two adjacent
148 atoms, which yielded 2631 unique angular parameters. These geometric parameters are rigorously
149 correlated with hydrogen adsorption Gibbs free energy (ΔG_{*H}) using Pearson correlation analysis,
150 with color mapping indicating correlation strength (dark red: strong positive, $r \approx +1$; dark blue:
151 strong negative, $r \approx -1$). Among these, the $\angle \text{S}_{17}\text{M}_{74}\text{S}_{22}$ angle exhibits the strongest correlation (r
152 = 0.75, Figures 2a; S4a-b), suggesting its potential as a HER activity descriptor. However, the
153 moderate correlation coefficient also reveals a fundamental limitation: dopant-centered angles,
154 being spatially localized, fail to fully capture the longer-range structural perturbations that
155 significantly influence catalytic behavior. This finding motivates us to explore the role of extended
156 coordination environments.

157 The influence of peripheral atomic arrangements on single-atom catalysts has been proposed
158 to arise from microstress variations that propagate across multiple coordination shells.^{29–31} Indeed,



159 metal doping not only modifies the electronic structure of the central active site but also induces
 160 long-range microstress fields that critically affect HER activity.^{46,47} To quantitatively test this
 161 hypothesis and develop more accurate structural descriptors, we extend our angle-based analysis
 162 to atoms residing in outer coordination shells surrounding the TM₁ centers.

View Article Online
 DOI: 10.1039/D6SC01740A



163
 164 **Figure 2. Correlation analysis of structural distortions with HER activity in TM₁@MoS₂-X.**
 165 (a-d) Pearson correlation coefficient (r) between ΔG_{H} and angles centered on (a) dopant atoms,
 166 (b) first-shell S atoms, (c) second-shell S atoms, and (d) Mo atoms. The angle exhibiting the
 167 strongest linear correlation is highlighted in each panel. (e-h) Linear relationship between the



168 optimal descriptor ϕ_{HER} and ΔG_{*H} across different substrates: (e) MoS₂, (f) WSe₂, (g) WS₂, and
169 (h) MoSe₂. Color scheme: (a-c) Structural representations showing the doped transition metal
170 center with first-shell S atoms in orange and second-shell S atoms in yellow. (d) Structural
171 representation showing the doped metal center with first-shell Mo atoms in light purple, second-
172 shell Mo in dark purple, third-shell Mo in green, and outermost-shell Mo in yellow.

174 To intuitively visualize the coordination environment, sulfur atoms in equivalent positions
175 are assigned identical colors, with gradation in shading representing increasing shell distance from
176 the active center (Figure 2a-d). Our systematic analysis reveals a significant trend: the correlation
177 with ΔG_{*H} strengthens as we move from the dopant center toward peripheral atomic shells. The
178 internal angle $\angle S_{23}S_{12}S_{42}$ exhibits a substantially improved correlation ($r = 0.82$; Figures 2b, S5a-
179 b), compared to dopant-centered descriptors. The trend becomes even more pronounced in the
180 second shell, where surface angle $\angle S_1S_{23}S_8$ shows an even stronger correlation ($r = 0.85$; Figures
181 2c, S6a-b), underscoring the critical role of peripheral effects in modulating catalytic performance.

182 To determine whether this phenomenon extends beyond sulfur-centered coordination, we
183 expand our analysis to angles centered on molybdenum atoms in outer shells. By applying
184 crystallographic symmetry principles, we systematically map Mo coordination environments
185 (Figures 2d; S7a-b) while maintaining consistent color-coding. Among these, the Mo-centered
186 internal angle $\angle S_{21}Mo_{65}Mo_{67}$ also demonstrates a strong correlation with HER activity ($r = 0.84$,
187 Figure 2d). Through a comprehensive comparison of all candidate descriptors, we identify the
188 second-shell surface angle $\angle S_1S_{23}S_8$, which exhibits the strongest overall correlation, as the
189 optimal angular descriptor for HER, designated ϕ_{HER} (Figure 2e). The consistent superiority of
190 peripheral-shell-centered angles over dopant-site-centered descriptors confirms that long-range
191 structural effects, rather than local metal-centered geometry, predominantly govern HER
192 performance in these SACs.

193 We further evaluate the transferability of ϕ_{HER} across different chalcogen-vacancy systems.
194 Impressively, this descriptor maintains strong linear correlations with ΔG_{*H} in TM₁@WS₂-S ($r =$
195 -0.83), TM₁@WSe₂-Se ($r = -0.83$), and TM₁@MoSe₂-Se ($r = -0.81$) (Figure 2f-h). Within the
196 TM₁@MoS₂-S system, Ir₁@MoS₂-S emerges as the optimal catalyst, with $\phi_{\text{HER}} = 26.99^\circ$
197 corresponding to a near-ideal ΔG_{*H} of -0.01 eV (Figure 2e). Similarly, Hf₁@WSe₂-Se, Ru₁@WS₂-
198 S, and Rh₁@MoSe₂-Se show superior HER activity in their respective systems, with ϕ_{HER} values
199 of 26.99° , 27.00° , and 26.96° , predicting ΔG_{*H} values of 0.06 , -0.04 , and 0.41 eV, respectively.
200 This consistent predictive accuracy across diverse material systems establishes ϕ_{HER} as a robust



201 and generalizable descriptor for structure-activity relationships. These results collectively reveal
202 the intrinsic mechanism of “periphery over core”: HER activity is more strongly correlated with
203 the geometric distortion of the peripheral coordination shell than with the locally doped center.
204 Additionally, they validate the good transferability of this type of angular descriptor across
205 different MX₂ hosts. This indicates that the doped atom acts merely as a trigger, while the long-
206 range structural response of the host lattice—quantified by specific peripheral angular
207 configurations—is the key determinant of catalytic performance.

View Article Online
DOI: 10.1039/D6SC01740A

208 **Transferability of Angular Descriptors from HER to OER**

209 We then aim to determine whether this angular descriptor approach could be extended to a
210 more complex reaction (OER). To evaluate the transferability of our descriptor framework, we
211 systematically analyze angle-overpotential relationships across the same family of chalcogen-
212 vacancy systems.

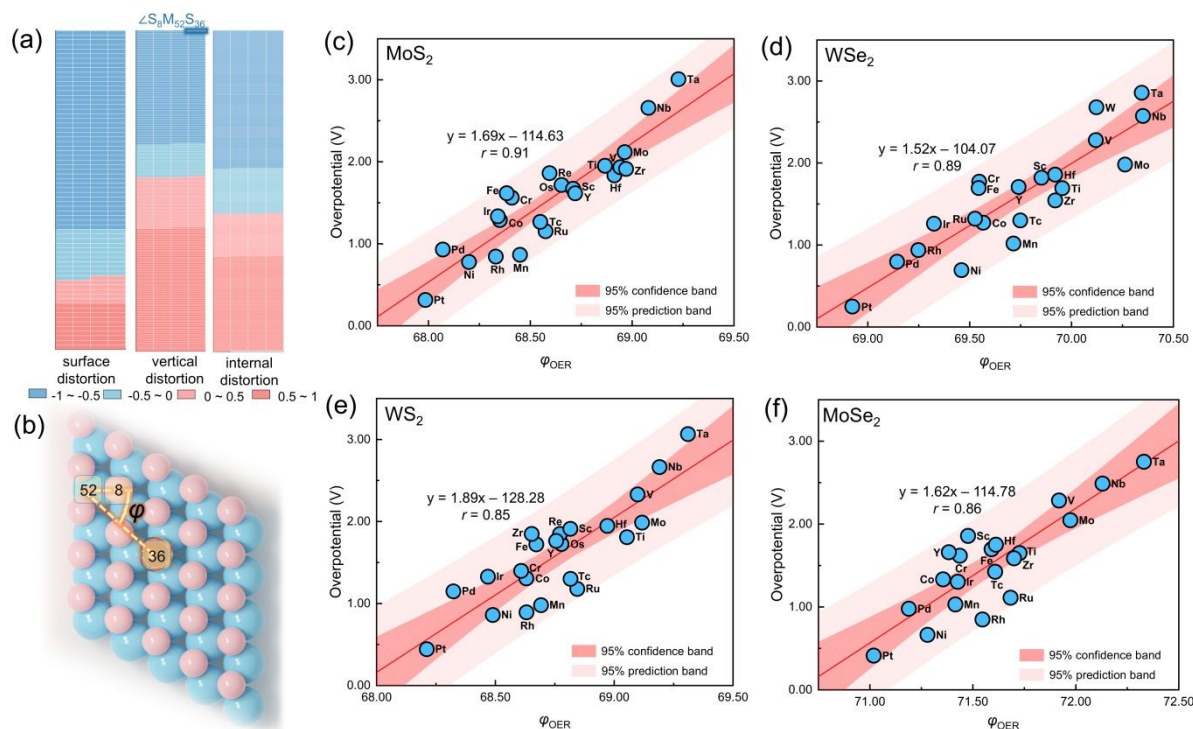
213 Initial screening of dopant-centered angles identifies $\angle S_1M_74S_6$ as the most promising
214 candidate ($r = 0.85$, Figure S8a-c). However, as observed with HER, extending our analysis to
215 peripheral coordination shells substantially enhances correlation strengths. First-shell sulfur-
216 centered angles, particularly the surface angle $\angle S_{15}S_{12}S_{19}$, exhibit a strong negative correlation
217 with OER overpotential ($r = -0.90$, Figure S9a-c), while second-shell sulfur-centered angles such
218 as $\angle S_{11}S_{23}S_{22}$ demonstrate an equally significant positive correlation ($r = 0.90$, Figure S10a-c),
219 indicating that smaller angles in this descriptor family favor enhanced OER activity.

220 Extending our analysis to Mo-centered angles in the outer coordination shells reveals that
221 the internal angle $\angle S_8Mo_{52}S_{36}$, centered on the outermost Mo₅₂ atom, exhibits a good correlation
222 ($r = 0.91$, Figure 3a), slightly exceeding all S-centered descriptors. We therefore establish this
223 Mo-centered angle as the optimal OER descriptor, designated φ_{OER} (Figure 3b). This descriptor
224 identifies Pt₁@MoS₂-S as the most promising catalyst within the TM₁@MoS₂-S system, with φ_{OER}
225 = 67.98° corresponding to a predicted overpotential of 0.51 V.

226 The robustness of φ_{OER} is confirmed through rigorous validation across four distinct material
227 systems though we note that experimental OER validation is not performed in the present
228 work: TM₁@MoS₂-S ($r = 0.91$), TM₁@WSe₂-Se ($r = 0.89$), TM₁@WS₂-S ($r = 0.85$), and
229 TM₁@MoSe₂-Se ($r = 0.86$) (Figure 3c-f). Among these, Pt₁@WSe₂-Se exhibits the highest
230 predicted activity with $\varphi_{OER} = 68.92^\circ$ corresponding to an overpotential of 0.36 V, while
231 Pt₁@WS₂-S ($\varphi_{OER} = 68.21^\circ$) and Pt₁@MoSe₂-Se ($\varphi_{OER} = 71.02^\circ$) show predicted overpotentials of
232 0.56 V and 0.60 V, respectively.



233 Our results demonstrate that the angular descriptor framework successfully transfers from
 234 HER to OER, revealing both universal principles and reaction-specific characteristics. While both
 235 optimal descriptors, φ_{HER} ($\angle\text{S}_1\text{S}_{23}\text{S}_8$) for HER and φ_{OER} ($\angle\text{S}_8\text{Mo}_{52}\text{S}_{36}$) for OER, exhibit strong
 236 correlations with their respective activities ($r = 0.85$ and 0.91), confirming that coordination shell
 237 geometry governs catalytic performance across different electrochemical reactions, OER displays
 238 significantly greater angular sensitivity. This is evidenced by both higher maximum correlation
 239 coefficients and a greater number of angles exhibiting $|r| > 0.8$. We attribute this enhanced
 240 sensitivity to the more complex OER mechanism, which involves multiple adsorbed intermediates
 241 along a convoluted reaction pathway, making it particularly susceptible to subtle geometric
 242 variations. Crucially, despite these mechanistic differences, both reactions adhere to a unified
 243 design principle in which dopants modulate catalytic activity primarily through long-range
 244 structural perturbations in peripheral environments rather than through local metal-centered
 245 effects. This fundamental understanding establishes angular descriptors as a universal strategy for
 246 geometry-informed catalyst design across diverse electrochemical processes.

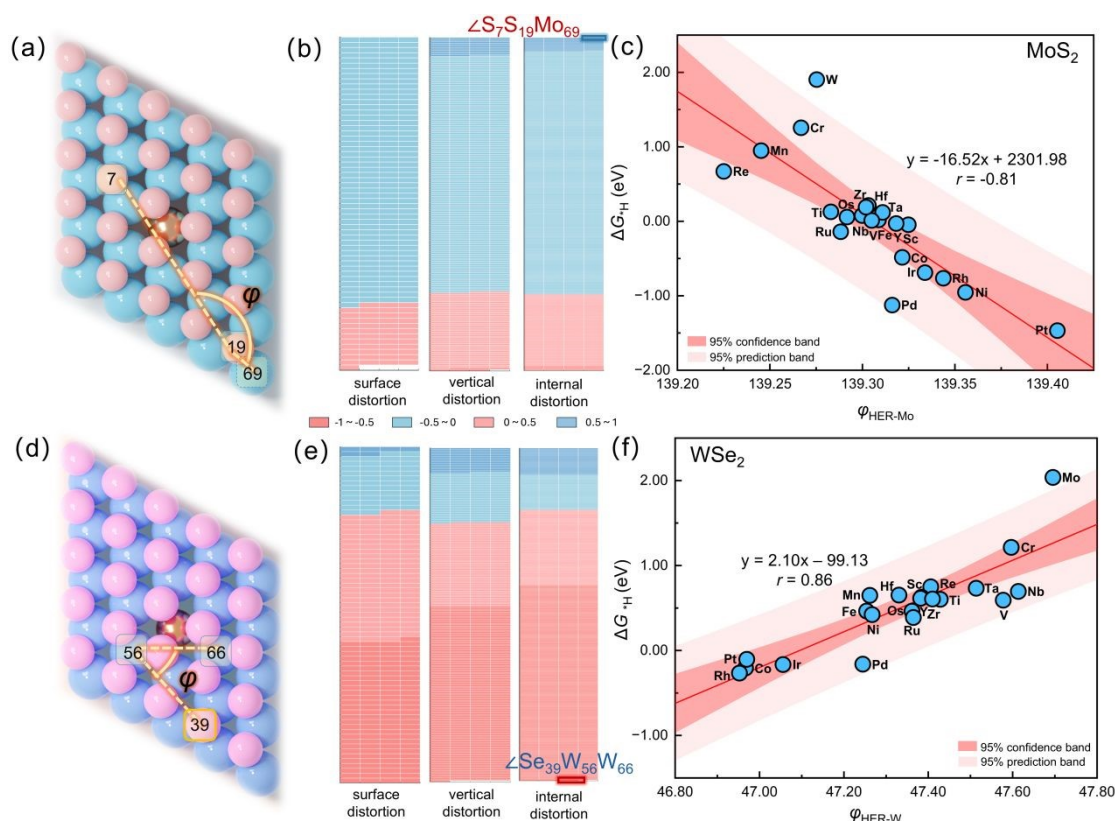


247
 248 **Figure 3. Angular descriptors for OER activity in $\text{TM}_1\text{@MX}_2\text{-X}$ systems.** (a) Correlation
 249 matrix of angle-overpotential relationships, identifying the internal angle of $\angle\text{S}_8\text{Mo}_{52}\text{S}_{36}$ as
 250 exhibiting the strongest correlation. (b) Atomic configuration of the optimal descriptor
 251 $\angle\text{S}_8\text{Mo}_{52}\text{S}_{36}$ (denoted as φ_{OER}). (c-f) Linear regression analysis demonstrating the robust
 252 correlation between φ_{OER} and OER overpotential across different substrates: (c) MoS_2 , (d) WSe_2 ,
 253 (e) WS_2 , and (f) MoSe_2 .

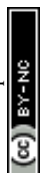


254 Transferability of Angular Descriptors from Chalcogen-Vacancy to Metal-Vacancy Systems DOI: 10.1039/D6SC01740A

255 After establishing the efficacy of angular descriptors in chalcogen-vacancy systems, we
 256 move on to investigate their applicability to the fundamentally distinct metal-vacancy
 257 configurations. MX_2 materials offer diverse doping sites,^{48,49} with surface chalcogen vacancies
 258 and subsurface metal vacancies representing two predominant configurations that yield
 259 substantially different reactive sites and catalytic behaviors.^{50,51} To assess the universal
 260 applicability of our descriptor framework, we extend our investigation to transition metal SACs
 261 formed by substituting Mo/W sites within the MX_2 lattice, which maintain the characteristic
 262 sandwich-like coordination geometry but position the active site differently (Figure 4a for MoS_2
 263 and Figure 4d for WSe_2 ; atomic labeling in Figure S7). In these metal-vacancy systems, reaction
 264 intermediates adsorb at surface chalcogen atoms rather than at the dopant site.



265
 266 **Figure 4. Angular descriptors for HER activity in $\text{TM}_1@MX_2$ (metal-vacancy) systems.** (a)
 267 Atomic configuration of the $\text{TM}_1@MoS_2\text{-Mo}$ showing the optimal angular descriptor $\angle S_7S_{19}Mo_{69}$,
 268 with blue, pink, and gold spheres representing Mo, S, and dopant atoms, respectively. (b)
 269 Correlation matrix of angle- ΔG^*_{H} correlation, identifying the internal angle of $\angle S_7S_{19}Mo_{69}$
 270 exhibiting the strongest negative correlation. (c) Linear regression analysis of the correlation
 271 between $\angle S_7S_{19}Mo_{69}$ and ΔG^*_{H} . (d) Atomic configuration of the $\text{TM}_1@WSe_2\text{-W}$ featuring the
 272 optimal descriptor $\angle S_{39}W_{56}W_{66}$, with purple, light red, and gold spheres representing W, Se, and



273 dopant atoms, respectively. (e) Correlation matrix identifying the internal angle of $\angle\text{Se}_{39}\text{W}_{56}\text{W}_{66}$
274 as showing the strongest positive correlation. (f) Linear regression analysis of the correlation
275 between $\angle\text{Se}_{39}\text{W}_{56}\text{W}_{66}$ and ΔG^*_{H} .

276
277 Our descriptor mining methodology proves equally effective in identifying key angular
278 parameters within these metal-vacancy systems. Through systematic coordination shell analysis,
279 we visualize the correlation landscape using a color-coded scheme (Figure 4b and 4e), where dark
280 red ($r = -1$ to -0.5) and dark blue ($r = 0.5$ to 1) represent the strongest correlations. This analysis
281 reveals two highly predictive angular descriptors: $\phi_{\text{HER-Mo}}$ (an internal angle of $\angle\text{S}_7\text{S}_{19}\text{Mo}_{69}$ in
282 MoS_2 systems, Figure 4b) and $\phi_{\text{HER-W}}$ (an internal angle of $\angle\text{Se}_{39}\text{W}_{56}\text{W}_{66}$ in WSe_2 , Figure 4e),
283 collectively designated as $\phi_{\text{HER-M}}$. These descriptors exhibit robust yet fundamentally distinct
284 correlations with ΔG^*_{H} . Specifically, $\phi_{\text{HER-Mo}}$ displays a significant negative correlation ($r = -0.81$),
285 where larger angles correspond to enhanced HER activity (Figure 4c). Accordingly, $\text{V}_1@\text{MoS}_2$ -
286 Mo emerges as the most active catalyst in this series with $\phi_{\text{HER-Mo}} = 139.31^\circ$ and a near-optimal
287 $\Delta G^*_{\text{H}} = 0.01$ eV, while the least active $\text{Pt}_1@\text{MoS}_2$ -Mo shows $\phi_{\text{HER-Mo}} = 139.41^\circ$ with a strongly
288 binding ΔG^*_{H} of -1.65 eV. Conversely, $\phi_{\text{HER-W}}$ demonstrates a strong positive correlation ($r =$
289 0.86), where increasing angular values improve catalytic performance (Figure 4f). The optimal
290 $\text{Ir}_1@\text{WSe}_2$ -W displays $\phi_{\text{HER-W}} = 47.06^\circ$ with $\Delta G^*_{\text{H}} = -0.08$ eV, whereas $\text{Mo}_1@\text{WSe}_2$ -W, which
291 shows the lowest HER activity, exhibits $\phi_{\text{HER-W}} = 47.70^\circ$ with $\Delta G^*_{\text{H}} = 1.26$ eV.

292 The consistently high correlation strengths (average $|r| > 0.8$) across both vacancy types
293 establish the universal predictive power and good transferability of angular descriptors in
294 $\text{TM}_1@\text{MX}_2$ catalysts. However, we observe a fundamental distinction in descriptor behavior
295 between the two systems: chalcogen-vacancy systems employ a universal descriptor ($\phi_{\text{HER}} =$
296 $\angle\text{S}_1\text{S}_{23}\text{S}_8$) across all catalysts, whereas in metal-vacancy systems, different atomic angles serve
297 as the key descriptors, such as $\angle\text{S}_7\text{S}_{19}\text{Mo}_{69}$ and $\angle\text{Se}_{39}\text{W}_{56}\text{W}_{66}$. This divergence in correlation
298 patterns stems from fundamental differences in how the two vacancy types perturb the electronic
299 structure, a phenomenon we quantitatively explore in the following electronic structure
300 investigation.

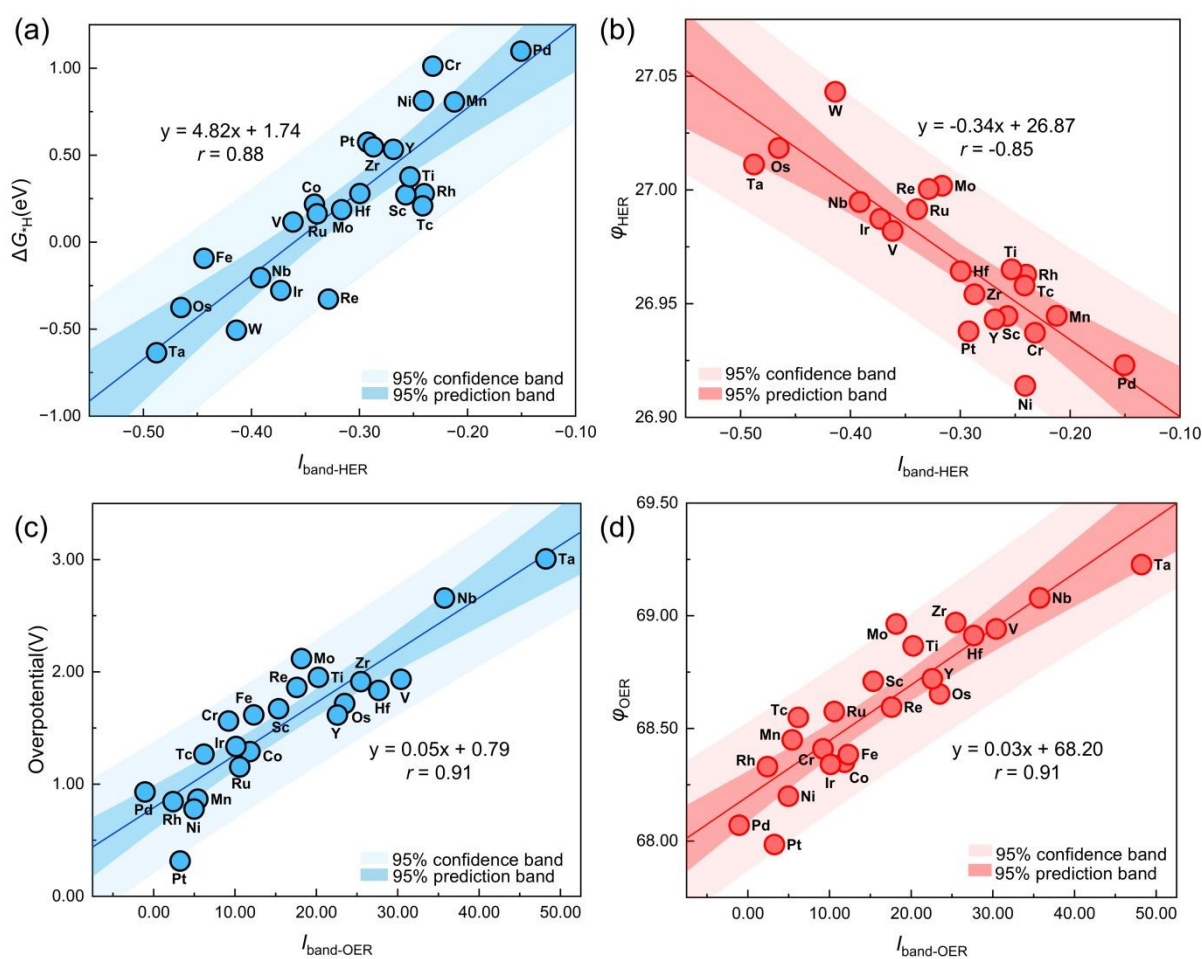
301 Electronic Origins of Angle-Activity Relationships

302 The established correlations between angular descriptors and catalytic activity prompt us to
303 investigate their underlying electronic origins. While the connection between structural distortions
304 and catalytic performance is known to be mediated by electronic structure,⁵²⁻⁵⁴ conventional
305 electronic descriptors show limited effectiveness in single-atom systems. Our systematic density



of states (DOS) analysis of $\text{TM}_1@ \text{MoS}_2\text{-S}$ reveals the inadequacy of the conventional d -band center (ϵ_d) theory for SACs. As shown in Figure S11-S12, ϵ_d shows only weak correlations with both HER (ΔG_{H} , $r = -0.30$) and OER (overpotential η , $r = 0.32$) activity. This limitation likely originates from fundamental characteristics of SACs: (i) anisotropic d -orbital/adsorbate interactions create orientation-dependent binding energies that are averaged out in ϵ_d analysis; (ii) the localized nature of catalytic activity in SACs depends on specific orbital contributions rather than global d -band properties. These observations underscore the need for descriptors that can bridge atomic-scale geometry with electronic structure—not as a replacement for all existing descriptors, but as an additional perspective.

To address these limitations, we develop a multidimensional descriptor framework integrating d -band and p -band center theory with our angular descriptors (ϕ_{HER} and ϕ_{OER}).^{55,56} Inspired by the binary descriptor approach,³² we apply the SISSO algorithm⁵⁷ to derive band-structure descriptors $I_{\text{band-HER}}$ and $I_{\text{band-OER}}$. These incorporate s -, p -, and d -band contributions from both dopant TM_1 ($\epsilon_{\text{M-s}}$, $\epsilon_{\text{M-d}}$) and surrounding atoms ($\epsilon_{23\text{-p}}$, $\epsilon_{1\text{-s}}$, $\epsilon_{36\text{-p}}$, $\epsilon_{52\text{-s}}$).



320



321 **Figure 5. Correlations between composite electronic descriptors and catalytic activities for**
 322 **TM₁@MoS₂-S.** (a) Linear relationship between $I_{\text{band-HER}}$ and ΔG_{*H} . (b) Linear correlation between
 323 $I_{\text{band-HER}}$ and the optimal angular descriptor $\angle S_1 S_{23} S_8$ (φ_{HER}). (c) Linear relationship between $I_{\text{band-}}$
 324 OER and OER overpotential. (d) Linear correlation between $I_{\text{band-OER}}$ and the optimal angular
 325 descriptor $\angle S_8 \text{Mo}_{52} S_{36}$ (φ_{OER}).
 326

327 The $I_{\text{band-HER}}$ descriptor shows an outstanding correlation with ΔG_{*H} ($r = 0.88$, Figure 5a) and
 328 a strong anti-correlation with φ_{HER} ($r = -0.85$, Figure 5b). These dual correlations reveal a coherent
 329 structure-activity relationship: while individual orbital bands provide incomplete activity
 330 descriptions, the integrated $I_{\text{band-HER}}$ descriptor captures essential electronic features governing
 331 HER performance, including band-center positions, bandwidth distributions, and multi-orbital
 332 coupling. More importantly, these results establish a fundamental mechanistic link: geometric
 333 distortions directly modulate the catalyst's electronic band structure, which in turn regulates ΔG_{*H}
 334 through coordinated s -, p -, and d -orbital interactions. This provides an atomic-level understanding
 335 of how structural modifications drive catalytic enhancements in TM₁@MX₂-X systems.

$$I_{\text{band-HER}} = \frac{\varepsilon_{\text{M-s}} + \varepsilon_{23\text{-p}}}{\varepsilon_{\text{M-d}} + \varepsilon_{1\text{-s}}}, \quad (1)$$

336 where $\varepsilon_{\text{M-s}}$ and $\varepsilon_{\text{M-d}}$ represent the s and d -band center values of the doped metal TM₁, respectively;
 337 $\varepsilon_{23\text{-p}}$ and $\varepsilon_{1\text{-s}}$ represent the p -band center value of atom S₂₃ and the s -band center value of atom S₁
 338 in angle $\angle S_1 S_{23} S_8$, respectively (Table S1-4).
 339

340 Extending our descriptor framework to OER, the composite descriptor $I_{\text{band-OER}}$ integrates
 341 key electronic features: $\varepsilon_{\text{M-s}}$ and $\varepsilon_{\text{M-d}}$ represent the s - and d -band centers of the dopant TM₁, while
 342 $\varepsilon_{36\text{-p}}$ and $\varepsilon_{52\text{-s}}$ correspond to the p -band center of S₃₆ and s -band center of Mo₅₂ within the
 343 $\angle S_8 \text{Mo}_{52} S_{36}$ angular configuration. Remarkably, $I_{\text{band-OER}}$ demonstrates good dual linear
 344 correlations with both φ_{OER} and OER overpotential, achieving identical correlation coefficients
 345 of $r = 0.91$ (Figure 5c-d). These robust relationships establish that dopant-induced structural
 346 modifications systematically alter catalyst geometry, which linearly modulates OER activity
 347 through well-defined electronic structure changes.

$$I_{\text{band-OER}} = (\varepsilon_{\text{M-d}} - \varepsilon_{36\text{-p}}) \times \varepsilon_{\text{M-s}} \times \varepsilon_{52\text{-s}}, \quad (2)$$

348 The versatility of our electronic descriptor framework is further demonstrated by its
 349 successful application to metal-vacancy systems. For TM₁@MoS₂-Mo, $I_{\text{band-Mo}}$ incorporates $\varepsilon_{\text{M-s}}$
 350 and $\varepsilon_{\text{M-d}}$ from the dopant TM₁, along with $\varepsilon_{19\text{-p}}$ and $\varepsilon_{69\text{-s}}$ (p -band center of S₁₉ and s -band center of
 351 S₆₉) derived from the key angle $\angle S_7 S_{19} \text{Mo}_{69}$ (Table S5). $I_{\text{band-Mo}}$ exhibits a significant correlation



352 with ΔG_{*H} ($r = 0.71$, Figure S13) and a strong anti-correlation with $\phi_{\text{HER-Mo}}$ ($r = -0.67$, Figure
 353 S14). Similarly, for $\text{TM}_1@WS_2\text{-W}$, $I_{\text{band-W}}$ integrates $\varepsilon_{\text{M-p}}$ (p -band center of TM_1) and ε_{56-d} (d -band
 354 center of W_{56}) from $\angle\text{Se}_{39}\text{W}_{56}\text{W}_{66}$ (Table S6), demonstrating strong anti-correlations with both
 355 ΔG_{*H} ($r = -0.85$, Figure S15) and $\phi_{\text{HER-W}}$ ($r = -0.80$, Figure S16).

$$I_{\text{band-Mo}} = \frac{\varepsilon_{19-p} - \varepsilon_{\text{M-s}}}{\varepsilon_{\text{M-d}} - \varepsilon_{69-s}}, \quad (3)$$

$$I_{\text{band-W}} = \left| e^{\varepsilon_{56-p}} - \frac{\varepsilon_{\text{M-s}}}{\Delta G_{*H}} \right|, \quad (4)$$

357 Our electronic structure analysis provides a unified mechanistic understanding of the
 358 observed descriptor behaviors across different vacancy types. Quantitative analysis reveals that
 359 metal doping induces markedly different electronic perturbations in the two systems: d -band
 360 center shifts of 0.008-0.640 eV in chalcogen-vacancy systems (Table S7), compared to
 361 substantially larger shifts of 0.013 to 1.760 eV in metal-vacancy systems (Table S8). This order-
 362 of-magnitude difference in electronic perturbation directly manifests in the geometric structure,
 363 explaining why angular descriptors exhibit limited transferability between vacancy types while
 364 maintaining strong predictive power within each category. Importantly, these results successfully
 365 resolve the “structural distortion \rightarrow electronic structure \rightarrow catalytic activity” causal chain in
 366 $\text{TM}_1@MX_2$ catalysts through electronic descriptors that surpass conventional single-parameter
 367 approaches.

368 Reliability Assessment

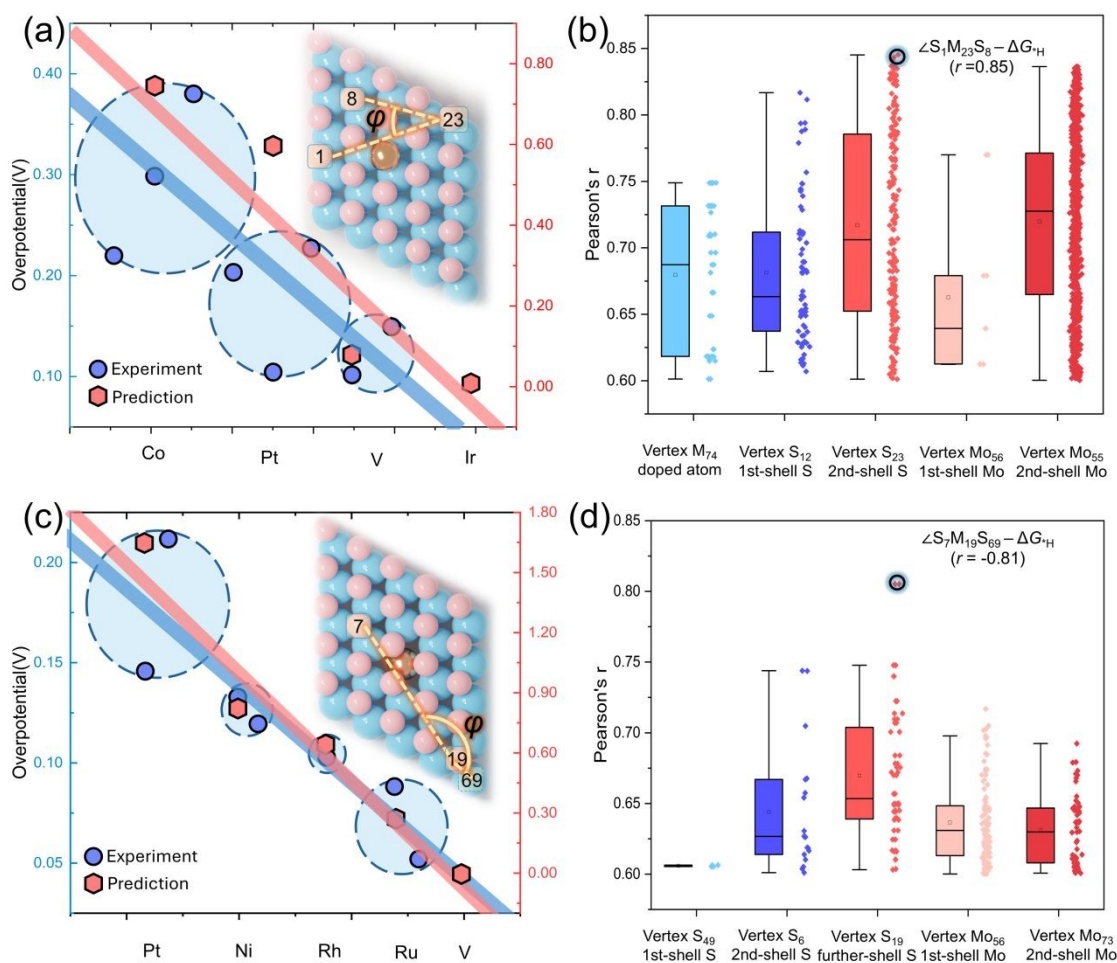
369 To rigorously evaluate the predictive accuracy of our angular descriptors, we perform
 370 systematic comparisons between descriptor-estimated catalytic activities and their corresponding
 371 DFT-computed values across all descriptor families: ϕ_{HER} (Figure S17-20), ϕ_{OER} (Figure S21-24),
 372 and $\phi_{\text{HER-M}}$ (Figure S25-26). The predictive performance is quantified by analyzing the slopes
 373 between predicted and computed values, where slopes approaching unity indicate superior
 374 accuracy. Our analysis demonstrates that all angular descriptors exhibit remarkable agreement
 375 with DFT benchmarks, confirming their reliability for catalytic activity prediction.

376 We further evaluate the practical utility of our framework by comparing descriptor-predicted
 377 activity trends with experimentally measured performances from published studies. Experimental
 378 overpotentials, compiled as averaged values from previous studies, are benchmarked against
 379 theoretical predictions obtained by converting ΔG_{*H} to overpotential via $\eta = |\Delta G_{*H}|/e$. As shown in
 380 Figure 6a, theoretical predictions for $\text{Co}_1@MoS_2\text{-S}$,^{34,58,59} $\text{Pt}_1@MoS_2\text{-S}$,⁶⁰⁻⁶² $\text{V}_1@MoS_2\text{-S}$,⁶³ and
 381 $\text{Ir}_1@MoS_2\text{-S}$ align well with experimental trends. Notably, $\text{Ir}_1@MoS_2\text{-S}$ is predicted to exhibit
 382 good HER activity with an overpotential of only 0.11 V. Correspondingly, as shown in Figure



383 S27, Ru₁@MoS₂-S,⁶⁴ Co₁@MoS₂-S,⁶⁵ and Ni₁@MoS₂-S⁶⁶ show good agreement with the OER
 384 performance trends experimentally measured in the literature. Among them, Pt₁@MoS₂-S
 385 demonstrates optimal OER performance at 0.29 V, which aligns with experimental report of Pt
 386 SAC as efficient OER materials,⁶⁷ providing independent validation of our descriptor approach.
 387 These results validate the predictive capacity of our angular descriptors and establish a rational
 388 foundation for dopant selection in catalyst synthesis.

389 To investigate the spatial dependence of descriptor effectiveness, we systematically analyze
 390 angular descriptors centered on five representative atomic sites across coordination shells: the
 391 dopant M₇₄, first-shell S₁₂, second-shell S₂₃, first-shell Mo₅₆, and second-shell Mo₅₅. Considering
 392 only angles with meaningful correlations ($|r| > 0.6$, Figure 6b), we observe that second-shell-
 393 centered angles are substantially more abundant than those from dopant or first-shell sites and
 394 exhibit higher average correlation coefficients. This spatial analysis definitively demonstrates that
 395 structural perturbations beyond the first coordination shell exert more substantial influence on
 396 HER activity than local metal-centered geometries.



397



398 **Figure 6. Reliability assessment of angular descriptors.** (a) Comparison between experimental
 399 measurements and ϕ_{HER} -predicted HER overpotential in chalcogen-vacancy systems. Blue and red
 400 lines represent fits to experimental and predicted values, respectively. (b) Correlation distributions
 401 for angles centered on different atomic sites (from left to right): dopant atom (M_{74}), first-shell
 402 sulfur (S_{12}), second-shell sulfur (S_{23}), first-shell molybdenum (Mo_{56}), and second-shell
 403 molybdenum (Mo_{55}). Box plots show statistical variations while overlaid curves indicate normal
 404 distributions. (c) Comparison between experimental measurements and $\phi_{\text{HER-Mo}}$ -predicted HER
 405 overpotential in metal-vacancy systems, with blue and red lines representing experimental and
 406 predicted fits, respectively. (d) Correlation distributions for angles centered on different atomic
 407 sites in metal-vacancy systems (from left to right): first-shell sulfur (S_{49}), second-shell sulfur (S_6),
 408 further-shell sulfur (S_{19}), first-shell molybdenum (Mo_{56}), and second-shell molybdenum (Mo_{73}).
 409

410 The predictive power of angular descriptors is further validated in metal-vacancy systems
 411 through comparison of $\phi_{\text{HER-Mo}}$ -derived overpotentials with experimental values. The strong
 412 agreement between predictions and measurements for $Pt_1@MoS_2-Mo$,^{35,68} $Ni_1@MoS_2-Mo$,^{69,70}
 413 $Rh_1@MoS_2-Mo$,⁷¹ and $Ru_1@MoS_2-Mo$ ^{70,72} confirms descriptor transferability across vacancy
 414 types, with $V_1@MoS_2-Mo$ exhibiting solid predicted HER activity (Figure 6c). Supplementary
 415 analysis (Figure 6d) filtering for angles with overpotential correlation $|r| > 0.6$ reveals that
 416 descriptors centered on outer-shell atoms are not only more numerous but also show stronger
 417 correlations, further highlighting the dominance of peripheral environments. While there is an
 418 optimal descriptor for HER, the results also indicate that some other angles exhibit good
 419 descriptive performance. The relatively reduced number of effective descriptors ($|r| > 0.6$) in Mo-
 420 vacancy systems compared to S-vacancy systems may originate from smaller atomic size
 421 mismatch between dopant and host metal atoms, resulting in less pronounced lattice distortions
 422 than those generated at chalcogen vacancy sites.

423 **Experimental Verification by Case Studies over $Ir_1@MoS_2$ and $V_1@MoS_2$**

424 Guided by computational predictions identifying $Ir_1@MoS_2$ (S-vacancy) and $V_1@MoS_2$
 425 (Mo-vacancy) as notable candidates, we synthesized these SACs with controlled atomic
 426 dispersion. X-ray diffraction (XRD) patterns (Figure S28) confirm the phase purity of all samples.
 427 Notably, the characteristic diffraction peaks for $V_1@MoS_2$ and $Ir_1@MoS_2$ exhibit a slight but
 428 consistent shift toward lower angles compared to pristine MoS_2 , which is indicative of lattice
 429 expansion induced by the doping of single-atom metal species into the MoS_2 matrix.^{35,73}
 430 Aberration-corrected high-angle annular dark-field scanning transmission electron microscopy

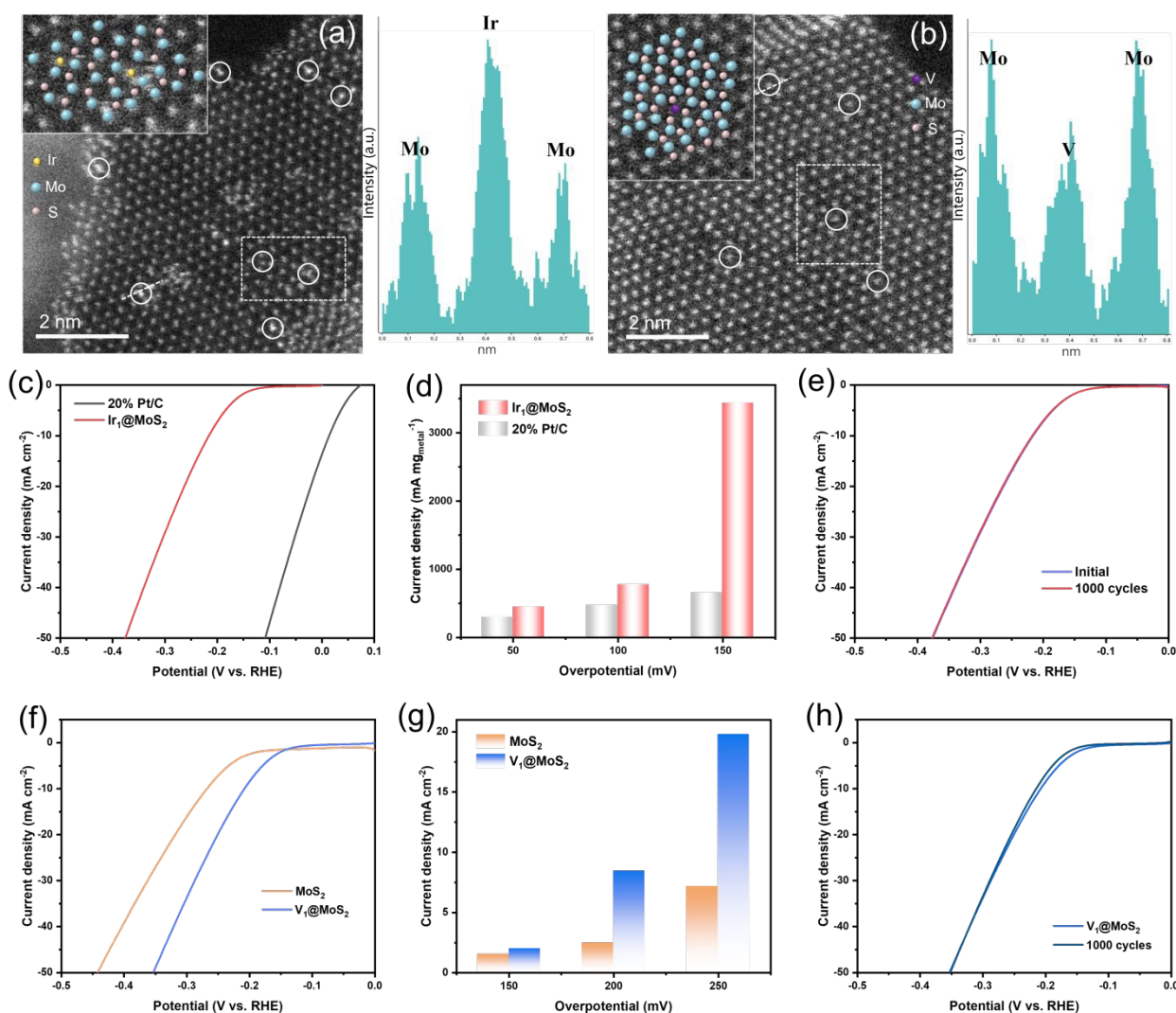


431 (AC HAADF-STEM) images provide direct visual evidence of single-atom dispersion state
432 which are consistent with Ir atoms occupying S-vacancy sites (Figure 7a) and V atoms substituting
433 the Mo sites (Figure 7b). In addition, X-ray photoelectron spectroscopy (XPS) was performed to
434 identify the electronic states. As shown in Figure S29, the Ir 4f_{7/2} binding energy for Ir₁@MoS₂
435 is 62.70 eV, consistent with the oxidation state of Ir species. These configurations are consistent
436 with our theoretically modelled TM₁@MX₂-X and TM₁@MX₂-M structures (Figure 1b, c). The
437 corresponding intensity line profiles (Figure 7a, b insets) quantitatively corroborate the atomic-
438 scale substitution, showing contrast variations consistent with the atomic numbers of the dopants
439 (Ir, V) relative to the host atoms (S, Mo). We note that while AC HAADF-STEM provides direct
440 visualization of single-atom dispersion and allows site assignment based on atomic number
441 contrast, the precise local coordination remains inferred from microscopy contrast and image
442 analysis.

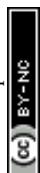
443 The HER performance of Ir₁@MoS₂ was evaluated in an acidic electrolyte. Despite an
444 ultralow loading of only 0.1 wt% Ir, this catalyst exhibits good activity, achieving a low
445 overpotential of ~0.22 V at a current density of 10 mA cm⁻² (Figure 7c). With increasing content
446 of Ir, the overpotential at 10 mA cm⁻² decreases from 220 mV at 0.05% Ir to 216 mV at 0.1% Ir,
447 then increases to 227 mV at a higher Ir content of 0.3% (Figure S30). At the same time, the current
448 densities at identical overpotentials present a volcanic trend with increasing Ir content. The
449 optimum Ir content of 0.1% (Ir₁@MoS₂) leads to the highest HER activity. This performance
450 is competitive with commercial Pt catalysts under identical conditions. To account for the minute
451 precious metal content, we compared mass activities. As shown in Figure 7d, the mass activity of
452 Ir₁@MoS₂ at -0.05 V vs. RHE compares favorably with that of a commercial Pt/C catalyst
453 with >20 wt% Pt loading. The electrochemically active surface area (ECSA), estimated via
454 double-layer capacitance (C_{dl}) measurements (Figure S31), increased from 16.4 mF cm⁻² for
455 pristine MoS₂ to 25.6 mF cm⁻² for Ir₁@MoS₂, indicating a greater density of accessible active
456 sites. Furthermore, Ir₁@MoS₂ demonstrates good stability, maintaining its activity through 1000
457 continuous cyclic voltammetry cycles (Figure 7e). Moreover, electrochemical impedance
458 spectroscopy (EIS) was employed to gain further insight into reaction kinetics and mechanisms.
459 The charge transfer resistance (R_{ct}) was related to the electrocatalytic kinetics and its lower value
460 corresponding to the faster reaction rate. Compared with MoS₂, Ir₁@MoS₂ possesses the lowest
461 charge transfer resistance (Figure S32). These results demonstrate that an ultralow content of Ir is
462 essential to induce a high HER activity. The reaction step diagram shows that in Ir₁@MoS₂-S, the
463 doped Ir₁ metal center site becomes the core active center for HER compared to other non-central
464 surface sites (Figure S33). Differential charge density and Bader charge analyses reveal that Ir₁



465 doping induces electron transfer from the surrounding Mo atoms to the Ir₁-H region,
 466 reconstructing the local electronic environment of MoS₂ and forming a strongly polarized
 467 adsorption site, thereby facilitating *H activation and enhancing HER performance (Figure S34).



468 **Figure 7. Structural characterization and electrocatalytic HER performance of Ir₁@MoS₂**
 469 **and V₁@MoS₂.** (a) Aberration-corrected HAADF-STEM image of Ir₁@MoS₂, with the
 470 corresponding linear intensity profile demonstrating Ir single-atom substitution at S sites (inset:
 471 the atom distribution of Ir, Mo, and S in panel a). (b) Aberration-corrected HAADF-STEM image
 472 of the V₁@MoS₂, with the corresponding linear intensity profile demonstrating V single-atom
 473 substitution at Mo sites (inset: the atom distribution of V, Mo, and S in panel b). (c) HER
 474 polarization curves for the Ir₁@MoS₂ (0.1 wt% Ir) and commercial 20% Pt/C samples. (d)
 475 Comparison of current densities for Ir₁@MoS₂ and 20% Pt/C at different overpotentials. (e)
 476 Stability test of Ir₁@MoS₂ before and after 1000 CV cycles. (f) HER polarization curves for
 477 V₁@MoS₂ and pristine MoS₂. (g) Comparison of current densities for V₁@MoS₂ and pristine
 478 MoS₂ at different overpotentials. (h) Stability test of V₁@MoS₂ before and after 1000 CV cycles.



480

View Article Online
DOI: 10.1039/D6SC01740A

481 The earth-abundant $V_1@MoS_2$ catalyst also shows a substantial enhancement in HER
482 activity compared to pristine MoS_2 . Linear sweep voltammetry (LSV) in Ar-saturated 0.5 M
483 H_2SO_4 shows that the overpotential required to achieve a current density of 10 mA cm^{-2} decreases
484 significantly from $\sim 0.27\text{ V}$ for pristine MoS_2 to $\sim 0.22\text{ V}$ for $V_1@MoS_2$ (Figure 7f). Across the
485 tested potential range, $V_1@MoS_2$ consistently delivers current densities that are 2 to 3 times higher
486 than those of the undoped baseline (Figure 7g). This activity boost is supported by an increased
487 C_{dl} value (Figure S31), suggesting a more favorable surface structure or improved
488 conductivity. $V_1@MoS_2$ also maintains good stability over 1000 CV cycles (Figure 7h),
489 demonstrating the inherent stability of the single-atom architecture within the MoS_2 lattice.

490 The exceptional experimental performance of both $Ir_1@MoS_2$ and $V_1@MoS_2$ provides strong
491 validation for our computational framework. We compare the HER performance of $Ir_1@MoS_2$
492 and $V_1@MoS_2$ with currently reported excellent catalysts. Our catalysts exhibit good activity
493 under ultra-low loading conditions, of which the intrinsic activity is superior to commercial Pt/C,
494 demonstrating competitive performance under ultralow loading conditions.^{58,62,74–77} These results
495 emphasize that the key outcome is the descriptor-guided discovery, as our angular descriptors
496 successfully led to experimentally active candidates and validated the predictive framework.
497 Together, these case studies complete a rigorous design cycle, from data-driven descriptor
498 discovery and theoretical screening to targeted synthesis and performance validation.

499 Discussion and Conclusions

500 The rational design of advanced catalysts is fundamentally limited by a translational gap: we
501 lack descriptors that are both predictive of activity and prescriptive for synthesis. While
502 electronic-structure-based parameters have advanced our understanding, they often fail to
503 translate into actionable geometric guidelines for experimentalists.^{15–19} Critically, even promising
504 structural descriptors, such as ensemble-averaged distortion metrics,²⁴ typically operate at a
505 macroscopic level. They capture the existence of lattice strain or distortion, long recognized as
506 crucial for catalysis, but lack the atomic-scale resolution to reveal which specific, local geometric
507 motifs are functionally decisive. This gap between observing macroscopic strain and deciphering
508 its atomically precise origins has hindered the development of a true “synthesis-to-function”
509 blueprint.

510 Our work bridges this gap by introducing angular descriptors as the missing link between
511 macroscopic lattice distortion and atomic-scale catalytic function. We propose that the doping-
512 induced macroscopic strains, often probed by techniques like HAADF-STEM and XRD, are

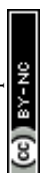


513 fundamentally manifested and quantifiable as precise changes in key structural angles within the
514 coordination network. Through systematic data mining of single-atom doped transition metal
515 dichalcogenides, we decode this relationship, developing interpretable angular parameters that
516 directly quantify how atomic-scale geometry governs catalytic activity. We demonstrate that
517 activity correlates more strongly with long-range angular parameters, such as the surface-oriented
518 angle $\angle S_1S_{23}S_8$ (ϕ_{HER}) and the internal torsion angle $\angle S_8Mo_{52}S_{36}$ (ϕ_{OER}), than with local
519 coordination environments. These structural descriptors exhibit both remarkable predictive
520 accuracy ($|r| > 0.81$ for HER, $|r| > 0.85$ for OER) and good transferability, precisely because they
521 capture the essential geometric signatures of functional strain.

522 A fundamental insight emerging from this decoding process is the dominant role of
523 peripheral structural environments over first-shell coordination spheres. This finding challenges
524 conventional design paradigms and provides a new geometric principle: catalytic activity is tuned
525 not merely by the immediate neighbors of the active site, but by how the dopant atom reconfigures
526 the entire local lattice. This geometric dominance is electronically rooted in multi-orbital
527 interaction mechanisms, which are quantitatively captured by our developed multidimensional
528 electronic descriptor (I_{band}). This descriptor demonstrates superior predictive power ($|r| = 0.88$ for
529 HER; $|r| = 0.91$ for OER) compared to conventional d -band theory, while providing a mechanistic
530 understanding of how geometric distortions modulate electronic states and adsorption energetics.

531 The practical utility of our framework is demonstrated through experimental validation.
532 Guided by our angular descriptors, we identified and synthesized $\text{Ir}_1@\text{MoS}_2$ (S-vacancy), which
533 achieves a low overpotential of 0.22 V at an ultralow loading of 0.1 wt%. When normalized by
534 precious metal content, the intrinsic activity surpasses that of commercial Pt/C catalysts
535 requiring >20 wt% Pt. Simultaneously, the earth-abundant $\text{V}_1@\text{MoS}_2$ (Mo-vacancy) exhibits
536 significantly enhanced HER activity compared to pristine MoS_2 . These successes are not isolated
537 discoveries; they are direct validations of the predictive framework that connects synthesizable
538 atomic-scale geometry (specific doping-induced angles) to targeted high performance.

539 In conclusion, this work establishes a generalizable geometric framework for single-atom
540 catalysis, demonstrating that “peripheral geometric regulation” applies across different reactions
541 and vacancy types. By decoding macroscopic lattice distortion into key angular descriptors, we
542 bridge the long-standing gap between structural effects and atomic-scale catalytic function.
543 Unlike previous electronic-model-confined studies, our angular signatures can serve as a
544 generalizable blueprint and predictors that show good transferability for the discovery of high-
545 performance single-atom electrocatalysts for sustainable hydrogen production. Nevertheless, its



546 applicability to other catalyst classes (e.g., alloy nanoparticles or metal surfaces) and to more
547 complex reaction networks remains to be explored.

View Article Online
DOI: 10.1039/D6SC01740A

548

549

550 **Author contributions**

551 B. G.:data curation, methodology, writing original draft, writing–review&editing; Y. C.:data
552 curation, methodology, writing original draft, writing–review&editing; Y. W.:data curation,
553 methodology, writing original draft, writing–review&editing; F. W.:visualization; F.
554 L.:visualization; L. C.:visualization; J. L.:conceptualization, funding acquisition, supervision,
555 project administration, writing–review&editing; X. F.:conceptualization, supervision, writing–
556 review&editing; S. L.:conceptualization, funding acquisition, supervision, writing–review&
557 editing.

558

559 **Data availability**

560 The detailed information for the theoretical calculations and additional experiments is provided
561 in the supplementary information (SI).

562

563 **Acknowledgments**

564 The present work was supported by the National Natural Science Foundation of China
565 (22461160253, 22373017, 22502083, 22508379 and 22378379), the National Natural Science
566 Foundation of Fujian Province of China (2024I0004), the “Chuying Program” for the Top Young
567 Talents of Fujian Province, the China Postdoctoral Science Foundation (2024M751372) and the
568 Jiangsu Funding Program for Excellent Postdoctoral Talent (2024ZB761). Part of DFT
569 computations were conducted at the Supercomputing Centre of Fujian.

570

571 **Conflict of Interest**

572 The authors declare no conflict of interest.

573

574 **Data Availability Statement**

575 The data are available upon reasonable request.

576

577 **References**



- 578 1 L.-M. Cao and C.-T. He, *Chin. J. Struct. Chem.*, 2026, **45**, 100814.
- 579 2 W. Shi, T. Shen, C. Xing, K. Sun, Q. Yan, W. Niu, X. Yang, J. Li, C. Wei, R. Wang, S. Fu,
580 Y. Yang, L. Xue, J. Chen, S. Cui, X. Hu, K. Xie, X. Xu, S. Duan, Y. Xu and B. Zhang, *Science*,
581 2025, **387**, 791–796.
- 582 3 H. Chen, L. Wang, M. Na and X. Zou, *Chem. Sci.*, 2025, **16**, 20662–20676.
- 583 4 H. Zeng, Z. Chen, Q. Jiang, Q. Zhong, Y. Ji, Y. Chen, J. Li, C. Liu, R. Zhang, J. Tang, X.
584 Xiong, Z. Zhang, Z. Chen, Y. Dai, C. Li, Y. Chen, D. Zhao, X. Li, T. Zheng, X. Xu and C. Xia,
585 *Nat. Commun.*, 2025, **16**, 4314.
- 586 5 Q. Deng, Z. Li, R. Huang, P. Li, H. Gomaa, S. Wu, C. An and N. Hu, *J. Mater. Chem. A.*,
587 2023, **11**, 24434–24453.
- 588 6 L. Chang, Z. Sun and Y. H. Hu, *Electrochem. Energ. Rev.*, 2021, **4**, 194–218.
- 589 7 Y. Liu, M. Han, Q. Xiong, S. Zhang, C. Zhao, W. Gong, G. Wang, H. Zhang and H. Zhao,
590 *Adv. Energy. Mater.*, 2019, **9**, 1803935.
- 591 8 M. Urso, X. Ju, R. Nittoor-Veedu, H. Lee, D. Zaoralová, M. Otyepka and M. Pumera, *ACS*
592 *Catal.*, 2025, **15**, 11617–11663.
- 593 9 S. Yuan, Y. Zheng, Y. Chu, C. Xia, R. Dong, J. Xu, B. Teng, Y. Wu and Y. He, *Green Energy*
594 *Environ.*, 2025, S246802572500189X.
- 595 10 J. Han, H. Wang, Y. Wang, H. Zhang, J. Li, Y. Xia, J. Zhou, Z. Wang, M. Luo, Y. Wang, N.
596 Wang, E. Cortés, Z. Wang, A. Vomiero, Z. Huang, H. Ren, X. Yuan, S. Chen, D. Feng, X. Sun,
597 Y. Liu and H. Liang, *Angew. Chem. Int. Ed.*, 2024, **63**, e202405839.
- 598 11 X. Li, J. Wang, H. Xue, L. Zhao, J. Lu, H. Zhang, M. Yan, F. Deng and C. Hu, *Adv. Funct.*
599 *Mater.*, 2025, **35**, 2503360.
- 600 12 T. Sun, T. Yang, W. Zang, J. Li, X. Sheng, E. Liu, J. Li, X. Hai, H. Lin, C. H. Chuang, C. Su,
601 M. Fan, M. Yang, M. Lin, S. Xi, R. Zou and J. Lu, *ACS Nano*, 2025, **19**, 5447–5459.
- 602 13 P. Cao, X. Mu, F. Chen, S. Wang, Y. Liao, H. Liu, Y. Du, Y. Li, Y. Peng, M. Gao, S. Liu, D.
603 Wang and Z. Dai, *Chem. Soc. Rev.*, 2025, **54**, 3848–3905.
- 604 14 M. Li, J. Li, X. Zheng and Y. Zhou, *Rare. Metals.*, 2024, **43**, 4019–4037.
- 605 15 A. A. Latimer, A. R. Kulkarni, H. Aljama, J. H. Montoya, J. S. Yoo, C. Tsai, F. Abild-
606 Pedersen, F. Studt and J. K. Nørskov, *Nat. Mater.*, 2017, **16**, 225–229.
- 607 16 F. Studt, F. Abild-Pedersen, T. Bligaard, R. Z. Sørensen, C. H. Christensen and J. K. Nørskov,
608 *Science*, 2008, **320**, 1320–1322.
- 609 17 J. Noh, S. Back, J. Kim and Y. Jung, *Chem. Sci.*, 2018, **9**, 5152–5159.
- 610 18 G. Cao, S. Yang, J.-C. Ren and W. Liu, *Nat. Commun.*, 2025, **16**, 1251.
- 611 19 J. Li, M. Chen, P. Wang, X. Li, Y. Huang, K. Ding, L. Mao, X. Xiang and X. Chen, *Chem.*
612 *Sci.*, 2025, **16**, 22071–22083.
- 613 20 X. Sun, R. B. Araujo, E. C. Dos Santos, Y. Sang, H. Liu and X. Yu, *Chem. Soc. Rev.*, 2024,
614 **53**, 7392–7425.
- 615 21 H. Xu, J. Wang, J. Liu and D. Cheng, *Acc. Chem. Res.*, 2025, **58**, 2535–2549.
- 616 22 J. Wang, M. Zheng, X. Zhao and W. Fan, *ACS Catal.*, 2022, **12**, 5441–5454.
- 617 23 M. Li, Y. Cheng, C. Shao and Y. Li, *Chin. J. Chem. Phys.*, 2025, **38**, 199–211.
- 618 24 R. Chattot, O. L. Bacq, V. Beermann, S. Köhl, J. Herranz, S. Henning, L. Kühn, T. Asset, L.
619 Guétaz, G. Renou, J. Drnec, P. Bordet, A. Pasturel, A. Eychmüller, T. J. Schmidt, P. Strasser, L.
620 Dubau and F. Maillard, *Nat. Mater.*, 2018, **17**, 827–833.
- 621 25 R. B. Wexler, J. M. P. Martirez and A. M. Rappe, *J. Am. Chem. Soc.*, 2018, **140**, 4678–4683.
- 622 26 C. Ren, Y. Cui, Q. Li, C. Ling and J. Wang, *J. Am. Chem. Soc.*, 2025, **147**, 13610–13617.
- 623 27 H. Xu, D. Cheng, D. Cao and X. C. Zeng, *Nat. Catal.*, 2024, **7**, 207–218.
- 624 28 W. Shu, J. Li, J. X. Liu, C. Zhu, T. Wang, L. Feng, R. Ouyang and W. X. Li, *J. Am. Chem.*
625 *Soc.*, 2024, **146**, 8737–8745.
- 626 29 F. Wei, L. Cao, B. Ge, Y. Chen, X. Pan, Y. Chai, R. Jing, X. Hu, X. Wang, J. Lin and S. Lin,
627 *Angew. Chem. Int. Ed.*, 2025, **64**, e202416912.
- 628 30 B. Ge, F. Wei, Q. Wan, H. Zhang, P. Yuan and S. Lin, *Precis. Chem.*, 2023, **1**, 429–436.



- 629 31 Y. Chai, F. Wei, L. Cao, X. Wang, S. Lin, J. Lin and T. Zhang, *Coord. Chem. Rev.*, 2025, **536**, 216649. View Article Online
DOI: 10.1039/D6SC01740A
- 630
- 631 32 Z. Han, R. Gao, T. Wang, S. Tao, Y. Jia, Z. Lao, M. Zhang, J. Zhou, C. Li, Z. Piao, X. Zhang
632 and G. Zhou, *Nat. Catal.*, 2023, **6**, 1073–1086.
- 633 33 C. Tang, L. Chen, H. Li, L. Li, Y. Jiao, Y. Zheng, H. Xu, K. Davey and S. Z. Qiao, *J. Am.*
634 *Chem. Soc.*, 2021, **143**, 7819–7827.
- 635 34 M. Pan, X. Zhang, C. Pan, J. Wang and B. Pan, *ACS Appl. Mater. Interfaces*, 2023, **15**,
636 19695–19704.
- 637 35 J. Xu, G. Shao, X. Tang, F. Lv, H. Xiang, C. Jing, S. Liu, S. Dai, Y. Li, J. Luo and Z. Zhou,
638 *Nat. Commun.*, 2022, **13**, 2193.
- 639 36 S. Wang, X. Ning, Y. Cao, R. Chen, Z. Lu, J. Hu, J. Xie and A. Hao, *Inorg. Chem.*, 2023, **62**,
640 6428–6438.
- 641 37 G. Liu, L. Ding, Y. Meng, A. Ali, G. Zuo, X. Meng, K. Chang, O. L. Li and J. Ye, *Carbon*
642 *Energy*, 2024, **6**, e521.
- 643 38 Z. Duan, H. Xia, H. Li, G. Shao, Y. Ren, X. Tang, Q. Liu, J. Hong, S. Dai, Y. Lin, K. Suenaga,
644 Y. He and S. Liu, *Rare Met.*, 2025, **44**, 3130–3140.
- 645 39 Z. Jiang, W. Zhou, C. Hu, X. Luo, W. Zeng, X. Gong, Y. Yang, T. Yu, W. Lei and C. Yuan,
646 *Adv. Mater.*, 2023, **35**, 2300505.
- 647 40 T. W. Clarkson and L. Magos, *Crit. Rev. Toxicol.*, 2006, **36**, 609–662.
- 648 41 L. Järup, *Br. Med. Bull.*, 2003, **68**, 167–182.
- 649 42 G. Kresse and J. Furthmüller, *Phys. Rev. B.*, 1996, **54**, 11169–11186.
- 650 43 C. Guan, X. Yue and Q. Xiang, *Adv. Mater.*, 2025, **37**, 2501209.
- 651 44 B. Zhou, B. Bai, X. Zhu, J. Guo, Y. Wang, J. Chen, Y. Peng, W. Si, S. Ji and J. Li, *J. Colloid*
652 *Interface Sci.*, 2024, **653**, 1177–1187.
- 653 45 X. B. Han, C. Q. Jing, H. Y. Zu and W. Zhang, *J. Am. Chem. Soc.*, 2022, **144**, 18595–18606.
- 654 46 Y. Liu, L. Xing, Y. Liu, D. Lian, M. Chen, W. Zhang, K. Wu, H. Zhu, Z. Sun, W. Chen, P.
655 Wu, D. Wang and Y. Ji, *Appl. Catal. B: Environ.*, 2024, **353**, 124088.
- 656 47 T. Zhang, Q. Ye, Y. Liu, Q. Liu, Z. Han, D. Wu, Z. Chen, Y. Li and H. J. Fan, *Nat. Commun.*,
657 2025, **16**, 3644.
- 658 48 Z. J. Duan, H. Xia, H. Z. Li, G. L. Shao, Y. Z. Ren, X. Tang, Q. N. Liu, J. H. Hong, S. Dai,
659 Y. C. Lin, K. Suenaga, Y. M. He and S. Liu, *Rare Met.*, 2025, **44**, 3130–3140.
- 660 49 Q. Jiang, H. Xu, K. S. Hui, Y. Wei, L. Liu, Z. Ye, C. Zha, M. Zheng, J. Lu and K. N. Hui,
661 *Adv. Mater.*, 2025, **37**, 2415986.
- 662 50 Z. Shi, X. Zhang, X. Lin, G. Liu, C. Ling, S. Xi, B. Chen, Y. Ge, C. Tan, Z. Lai, Z. Huang,
663 X. Ruan, L. Zhai, L. Li, Z. Li, X. Wang, G.-H. Nam, J. Liu, Q. He, Z. Guan, J. Wang, C. S. Lee,
664 A. R. J. Kucernak and H. Zhang, *Nature*, 2023, **621**, 300–305.
- 665 51 Y. Jia, Y. Zhang, H. Xu, J. Li, M. Gao and X. Yang, *ACS Catal.*, 2024, **14**, 4601–4637.
- 666 52 A. Gaur, J. Sharma, G. Kaur, S. Mhin and H. Han, *Adv. Funct. Mater.*, 2025, e16674.
- 667 53 C. Yin, F. Mo, X. Li, F. Li, W. Xue, Q. Wang, R. Shi, Y. Zhao, A. Zeb, J. Wang, W. Liu, S.
668 Zhan and Q. Zhou, *Appl. Catal. B: Environ.*, 2025, **376**, 125470.
- 669 54 R. Wang, L. Zhang, J. Shan, Y. Yang, J. Lee, T. Chen, J. Mao, Y. Zhao, L. Yang, Z. Hu and
670 T. Ling, *Adv. Sci.*, 2022, **9**, 2203917.
- 671 55 J. Wang, X. Li, B. Wei, R. Sun, W. Yu, H. Y. Hoh, H. Xu, J. Li, X. Ge, Z. Chen, C. Su and
672 Z. Wang, *Adv. Funct. Mater.*, 2020, **30**, 1908708.
- 673 56 Y. Wang, D. Wang, J. Gao, X. Hao, Z. Li, J. Zhou and F. Gao, *Phys. Chem. Chem. Phys.*,
674 2020, **22**, 14537–14543.
- 675 57 R. Ouyang, S. Curtarolo, E. Ahmetcik, M. Scheffler and L. M. Ghiringhelli, *Phys. Rev. Mater.*,
676 2018, **2**, 083802.
- 677 58 T. H. M. Lau, X. Lu, J. Kulhavy, S. Wu, L. Lu, T. S. Wu, R. Kato, J. S. Foord, Y. L. Soo, K.
678 Suenaga and S. C. E. Tsang, *Chem. Sci.*, 2018, **9**, 4769–4776.



- 679 59 S. Park, J. Park, H. Abroshan, L. Zhang, J. K. Kim, J. Zhang, J. Guo, S. Siahrostami and X.
680 Zheng, *ACS Energy Lett.*, 2018, **3**, 2685–2693. DOI: 10.1039/D6SC01740A
- 681 60 W. Yan, Z. Zhao, Z. Xin, J. Hu, J. Xia, L. Zhou, Y. Xu, Y. Zhang, K. Liu, R. Wang and Y.
682 Sun, *Adv. Funct. Mater.*, 2025, **35**, 2423262.
- 683 61 M. Li, J. Xu, D. Liu, J. Yang, J. Lin, X. Xiao, Z. Wang, X. Liu, L. Jia, Y. Liu, C. Yao, Y. Li,
684 Z. Lian and W. Yang, *Appl. Surf. Sci.*, 2024, **667**, 160384.
- 685 62 T. H. M. Lau, S. Wu, R. Kato, T. S. Wu, J. Kulhavý, J. Mo, J. Zheng, J. S. Foord, Y. L. Soo,
686 K. Suenaga, M. T. Darby and S. C. E. Tsang, *ACS Catal.*, 2019, **9**, 7527–7534.
- 687 63 S. Bolar, S. Shit, N. C. Murmu, P. Samanta and T. Kuila, *ACS Appl. Mater. Interfaces*, 2021,
688 **13**, 765–780.
- 689 64 V. H. Hoa, D. T. Tran, S. Prabhakaran, D. H. Kim, N. Hameed, H. Wang, N. H. Kim and J.
690 H. Lee, *Nano Energ.*, 2021, **88**, 106277.
- 691 65 X. Gong, Z. Jiang, W. Zeng, C. Hu, X. Luo, W. Lei and C. Yuan, *Nano Lett.*, 2022, **22**, 9411–
692 9417.
- 693 66 G. Wang, G. Zhang, X. Ke, X. Chen, X. Chen, Y. Wang, G. Huang, J. Dong, S. Chu and M.
694 Sui, *Small*, 2022, **18**, 2107238.
- 695 67 X. Xu, H. Xu and D. Cheng, *Nanoscale*, 2019, **11**, 20228–20237.
- 696 68 J. Deng, H. Li, J. Xiao, Y. Tu, D. Deng, H. Yang, H. Tian, J. Li, P. Ren and X. Bao, *Energy*
697 *Environ. Sci.*, 2015, **8**, 1594–1601.
- 698 69 J. Ge, Y. Chen, Y. Zhao, Y. Wang, F. Zhang and X. Lei, *ACS Appl. Mater. Interfaces*, 2022,
699 **14**, 26846–26857.
- 700 70 J. Ge, D. Zhang, Y. Qin, T. Dou, M. Jiang, F. Zhang and X. Lei, *Appl. Catal. B: Environ.*,
701 2021, **298**, 120557.
- 702 71 X. Meng, C. Ma, L. Jiang, R. Si, X. Meng, Y. Tu, L. Yu, X. Bao and D. Deng, *Angew. Chem.*
703 *Int. Ed.*, 2020, **132**, 10588–10593.
- 704 72 J. Wang, W. Fang, Y. Hu, Y. Zhang, J. Dang, Y. Wu, B. Chen, H. Zhao and Z. Li, *Appl.*
705 *Catal. B: Environ.*, 2021, **298**, 120490.
- 706 73 J. Zhu, Z. Wang, H. Yu, N. Li, J. Zhang, J. Meng, M. Liao, J. Zhao, X. Lu, L. Du, R. Yang,
707 D. Shi, Y. Jiang and G. Zhang, *J. Am. Chem. Soc.*, 2022, **139**, 10216–10219.
- 708 74 Y. Qu, B. Chen, Z. Li, X. Duan, L. Wang, Y. Lin, T. Yuan, F. Zhou, Y. Hu, Z. Yang, C. Zhao,
709 J. Wang, C. Zhao, Y. Hu, G. Wu, Q. Zhang, Q. Xu, B. Liu, P. Gao, R. You, W. Huang, L. Zheng,
710 L. Gu, Y. Wu and Y. Li, *J. Am. Chem. Soc.*, 2019, **141**, 4505–4509.
- 711 75 R. Zhang, Y. Li, X. Zhou, A. Yu, Q. Huang, T. Xu, L. Zhu, P. Peng, S. Song, L. Echegoyen
712 and F.-F. Li, *Nat. Commun.*, 2023, **14**, 2460.
- 713 76 H. Jiang, W. Yang, M. Xu, E. Wang, Y. Wei, W. Liu, X. Gu, L. Liu, Q. Chen, P. Zhai, X.
714 Zou, P. M. Ajayan, W. Zhou and Y. Gong, *Nat. Commun.*, 2022, **13**, 6863.
- 715 77 Y. Shi, W.-M. Huang, J. Li, Y. Zhou, Z.-Q. Li, Y.-C. Yin and X.-H. Xia, *Nat. Commun.*,
716 2020, **11**, 4558.
- 717



Data availability

View Article Online
DOI: 10.1039/D6SC01740A

The data supporting this article have been included as part of the article and Supplementary Information.

